

# Dynamic vs. Stationary Analysis of Electrochemical Carbon Dioxide Reduction: Profound Differences in Local States

Inga Dorner,<sup>[a]</sup> Philipp Röse,<sup>[a]</sup> and Ulrike Krewer\*<sup>[a]</sup>

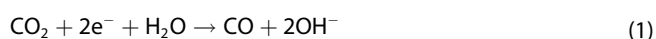
Electrochemical CO<sub>2</sub> reduction is crucial for mitigating emissions by converting them into valuable chemicals. Stationary methods suffer from drawbacks like gas bubble distortion and long measurement times. However, dynamic cyclovoltammetry in rotating disc electrode setups is employed to infer performance. This study uncovers limitations when applying this approach to CO<sub>2</sub> reduction in aqueous electrolyte. Here, we present a model-based analysis considering electrochemical reactions, species and charge transport, and chemical carbonation. Experimental and simulated potential cycles demonstrate scan rate dependence, significantly deviating from stationary curves at low rotation rates (50 rpm). Such low rotation rates mimic real diffusion layer thicknesses in practical cell systems, thus a

transport impact can be expected also on cell level. This behavior arises from slow transport and carbonation, causing time-dependent CO<sub>2</sub> depletion and electrolyte buffering. Dynamic investigation reveals strong species transport effects. Furthermore, dynamic operation enhances Faradaic efficiency due to a shift in the carbonate reaction system, favoring electrochemical CO<sub>2</sub> consumption over chemical CO<sub>2</sub> consumption. By clarifying dynamic vs. stationary operation, this research contributes to understanding electrochemical CO<sub>2</sub> reduction processes, how to determine transport limitations via dynamic measurements, and provides guidelines for more accurate performance assessment.

## Introduction

The electrochemical CO<sub>2</sub> reduction (CO<sub>2</sub>R) is a key technology for electrifying industrial processes, as it enables CO<sub>2</sub> to be recycled into valuable chemicals or fuels. It thus helps to close the carbon cycle and provides a non-fossil source of carbon.<sup>[1]</sup>

The challenge in electrochemical CO<sub>2</sub> reduction is to ensure high selectivity compared to the hydrogen evolution reaction (HER), which takes place in the same potential range. In addition, the low solubility of CO<sub>2</sub> in aqueous electrolyte limits the Faradaic current density for CO<sub>2</sub>R. At a silver catalyst in alkaline electrolyte, the following electrochemical reactions take place [Eq. (1) and (2)]:



Research on electrochemical CO<sub>2</sub>R covers a huge range of development aspects: catalyst development,<sup>[2–5]</sup> electrode structure optimization,<sup>[6,7]</sup> and cell and process design.<sup>[8,9]</sup>

Electrochemical analysis methods are widely used for characterization and performance evaluation at all three aspects. Experimental stationary analysis and models are widely used to determine kinetic parameters such as exchange current density and catalytic activity from Tafel plots and polarization curves.<sup>[10–12]</sup> A prerequisite for the comparability of catalyst materials is the investigation under defined mass transport conditions. For example, high rotation rates in rotating disk electrode setups avoid diffusion limitations.<sup>[13]</sup> However, studies show that the local reaction conditions of CO<sub>2</sub>R in aqueous bicarbonate electrolytes are strongly controlled by mass transport. The interplay between the electrochemical reactions, transport processes, and the chemical carbonate equilibrium leads to high complexity. Our previous studies on air operated alkaline membrane fuel cells showed that carbonation in the electrolyte is a slow process in a similar time range as migration or diffusion, leading to complex concentration profiles and pH changes near and at the electrodes.<sup>[14]</sup> This makes catalyst characterization and performance prediction challenging.<sup>[15]</sup> Thus, due to the strong influence of mass transport, it is essential to identify the hydrodynamic conditions of the cell setup. For steady-state measurements on silver electrodes, this has already been established.<sup>[13]</sup>

Steady-state polarization curves lack the ability to separate processes with similar time constants.<sup>[16]</sup> Additionally, they take a long time and the potential signal is disturbed by gas bubble formation for most gas-evolving reactions, such as oxygen and hydrogen evolution reactions,<sup>[17]</sup> chlorine evolution,<sup>[18]</sup> or CO<sub>2</sub> reduction.<sup>[19,20]</sup>

Dynamic analysis of the system provides a remedy for all these challenges. Dynamic analysis of mass transport is often carried out by chronoamperometry. Experimental observations of the current change during the applied potential steps can be

[a] I. Dorner, Dr. P. Röse, Prof. Dr.-Ing. U. Krewer  
Institute for Applied Materials – Electrochemical Technologies  
Karlsruhe Institute of Technology  
Adenauerring 20b, 76131 Karlsruhe (Germany)  
E-mail: ulrike.krewer@kit.edu

Supporting information for this article is available on the WWW under <https://doi.org/10.1002/celec.202300387>

© 2023 The Authors. ChemElectroChem published by Wiley-VCH GmbH. This is an open access article under the terms of the Creative Commons Attribution License, which permits use, distribution and reproduction in any medium, provided the original work is properly cited.

analyzed, for example, by the simple Cottrell equation<sup>[21,22]</sup> or by a physicochemical model when complex interactions such as phase change and diffusion of multiple species are involved.<sup>[23,24]</sup> Gupta *et al.* reported on a dynamic model including the diffusion of dissolved species for the electrochemical CO<sub>2</sub> reduction on a copper electrode. The transient state analysis via potential step and pulsed potentials showed a strong dependency of the local CO<sub>2</sub> concentration and pH on the diffusion layer thickness and on time.<sup>[25]</sup> The work emphasizes the importance of considering mass transport but needs to explain the reasons in detail. In-depth investigations of pulsed electrochemical reduction of CO<sub>2</sub> on copper have revealed the strong influence of pulsed potentials and their duration times on Faradaic efficiency for CO<sub>2</sub>R and C<sub>2+</sub> products. These studies highlight the significant impact on dynamic behavior of interacting processes within this reaction system which mainly defines the local state at the electrode.<sup>[26,27]</sup>

Dynamic methods such as cyclic voltammetry or electrochemical impedance spectroscopy (EIS) are well-known analysis techniques. But they are rarely used for quantifying mass transport or kinetic parameters in the electrochemical CO<sub>2</sub> reduction.<sup>[16]</sup> Their transient nature requires calculations and modeling effort when electrochemical reaction, mass transport processes and electrolyte effects are superimposed and interact. Nevertheless, these techniques, in combination with dynamic modeling, offer the possibility of separating and analyzing reaction kinetics and mass transport phenomena individually.<sup>[28]</sup> Impedance spectroscopy allows reaction and mass transport to be separated at a defined operating point; the reaction typically yields in a semicircle within a high-frequency range, while at low frequencies, a Warburg-type arc or straight line is observed.<sup>[29]</sup> Physicochemical models can provide insights into these processes and help to understand reaction and transport phenomena. For instance, they identify and explain inductive behavior at low frequencies caused by complex kinetics with adsorbed intermediates,<sup>[30]</sup> or heterogeneously flooded electrodes, which lead to a broad distribution of time constants.<sup>[31]</sup> For CO<sub>2</sub> reduction, Bienen *et al.* performed a comprehensive EIS analysis of electrochemical carbon dioxide reduction at tin electrodes.<sup>[32,33]</sup> Both, CO<sub>2</sub> reduction and competing HER, result in a combined, mixed time constant. A low-frequency process may be attributed to ionic transport but cannot be reliably identified.

Cyclic voltammograms allow better identification of reaction kinetic constants for multi-step reactions, including electrochemically coupled chemical reaction steps on the surface,<sup>[34]</sup> as reactions occur at specific potentials. They have also been used to identify reaction kinetics and parameters for multi-step reactions where homogeneous reactions occur in the electrolyte and where mass transport affects the measurement.<sup>[28]</sup> In addition, cyclic voltammetry provides rapid system analysis and is less affected by the perturbation of the current-potential-curve caused by gas evolution.

Besides the electrochemical reaction and mass transport processes, the pH-dependent carbonate equilibrium in the electrolyte plays an important role [Eq. (3)–(5)].



It significantly determines the local reaction conditions, such as CO<sub>2</sub> availability and pH value. It is concluded that knowledge about the kinetics of the buffer reactions is required because equilibrium conditions are not achieved in steady-state operation.<sup>[35]</sup> Dynamic analysis using differential electrochemical mass spectrometry confirms that the carbonate buffer reaction is an additional pathway of CO<sub>2</sub> consumption. It is observed experimentally only at slow scan rates <20 mVs<sup>-1</sup> and is suppressed at high scan rates. It is supposed that the occurrence of CO<sub>2</sub> consumption by carbonation at slow scan rates only results from the slow rate of the carbonate buffer reaction.<sup>[36]</sup> In addition, time-resolved pH measurements at gold electrodes in acidic 0.1 M Li<sub>2</sub>SO<sub>4</sub> observed a slow dynamic adaptation of the local pH value after potential steps.<sup>[37,38]</sup> A simulative study that clarifies the detailed interactions between reaction rates of carbonation, transport, and local reaction conditions has been lacking.

This study will show how to adjust conditions for dynamic operation for rapid and almost gas bubble-unaffected characterization of catalysts in electrochemical CO<sub>2</sub> reduction. Mass transport limitations can be easily revealed by varying the scan rate. Furthermore, the reasons for the discrepancy between the steady-state polarization curve and the cyclic voltammogram are explained using a dynamic physicochemical, experimentally validated model for CO<sub>2</sub> reduction on planar silver electrodes. By varying the rotation rates in rotating disc electrode setups, which imitates the effect of diffusion layers of real flow cell setups, it is shown that the hydrodynamic conditions strongly effect dynamic and steady-state performance. Insightful conclusions are derived for the interaction of transport processes, electrochemical reaction, and electrolyte reaction and their influence on current densities and Faradaic efficiency.

## Results and Discussion

### Dynamic vs. steady state behavior

In the following, differences between the dynamic and steady-state performance will be revealed, quantified and analyzed. The underlying differences in concentrations at the electrode that cause the performance differences will be explained.

The current evolution vs. potential during steady-state and cyclic voltammetry for different scan rates is given in Figure 1a for the experiments and in Figure 1b for the simulation. Progression of the steady-state and dynamic current curves is similar for experiment and simulation, whereas some quantitative trends between experiment and simulation are slightly different, in particular for the polarisation curve. Lower current densities for this curve compared to dynamic measurement in intermediate potential range, can be caused by stronger

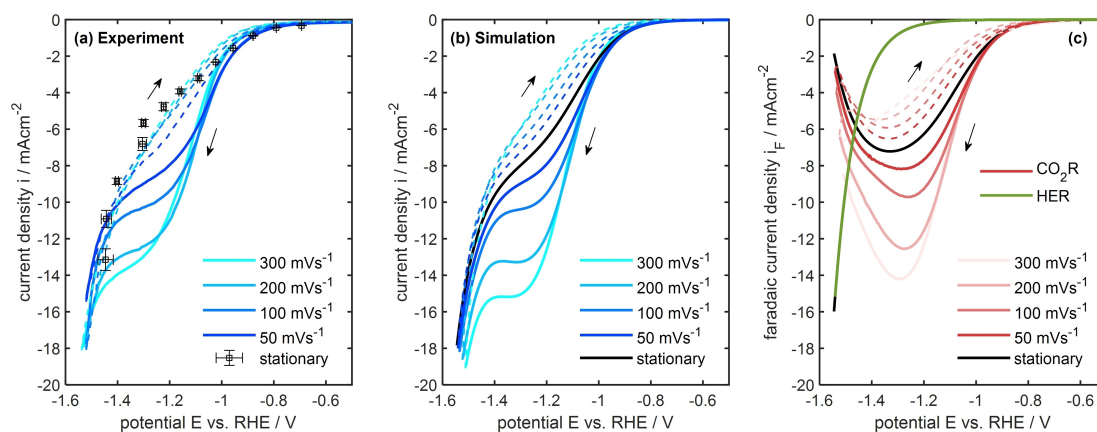


**Figure 1.** (a) Experimental and (b) simulated cyclic voltammograms for different scan rates and steady-state polarization curve. (c) Corresponding simulated Faradaic current densities for electrochemical CO<sub>2</sub> reduction (CO<sub>2</sub>R) and hydrogen evolution reaction (HER) as a function of potential. Forward sweeps are shown in solid lines and backward sweep in dashed lines. Conditions: CO<sub>2</sub> saturated 0.1 M KHCO<sub>3</sub> solution, room temperature, rotation rate of 50 rpm (corresponding to a diffusion layer thickness of 103 μm). Potentials are corrected for iR-drop.

limitation than expected in simulations or slightly overcorrected CV curves by iR-correction for experimental results.

The current density for the forward sweep of the CV and the polarization curve shows a similar behavior, namely an exponential decrease between  $-0.8$  to  $-1.2$  V, with a plateau in the potential range of  $-1.2$  to  $-1.4$  V, followed by a consecutive exponential decrease in current. No limiting current is observed in the potential window. Our simulations in Figure 1c show that the potential at which the plateau occurs coincides with a maximum in the Faradaic current for the CO<sub>2</sub>R. A similar observation was made experimentally by Hatsukade *et al.* in a flow cell setup and confirmed by product analysis.<sup>[39]</sup> Furthermore, our results show that, as the peak in Faradaic current density of CO<sub>2</sub> shifts to higher potentials for faster scan rates, the plateau in current density also shifts in the same direction. The CO<sub>2</sub> reduction is the prevalent electrochemical reaction at potentials between  $-0.8$  to  $-1.2$  V. At more negative potentials, the CO<sub>2</sub>R is suppressed mainly due to the depletion of CO<sub>2</sub> at the electrode surface, as shown in the simulation results, Figure 2a. The HER thus becomes the dominant reaction in the potential range below  $-1.4$  V. A large amount of electrolyte available for HER reaction explains the absence of a limiting current. While the trend of exponential behavior with an intermediate plateau is identical for all scan rates, a strong dependency of current density on the scan rate is observable in the experiments. The higher the scan rate, the more current density is measured at the same potential. This trend is well reproduced by the simulation. Further, experiment and simulation show similar trends in the backward sweep: In contrast to the clear plateau while decreasing potential, there is only a very weak plateau, which is rather a slight decrease in current slope. This correlates well with the lower CO<sub>2</sub> reduction rate and maximum in this region.

There is further a hysteresis between forward and backward sweep, which becomes more significant at higher scan rates. All these observations result in a discrepancy between stationary and dynamic current-potential curves. Simulation in Figure 1c shows that the scan rate dependence is very strong for CO<sub>2</sub>R,

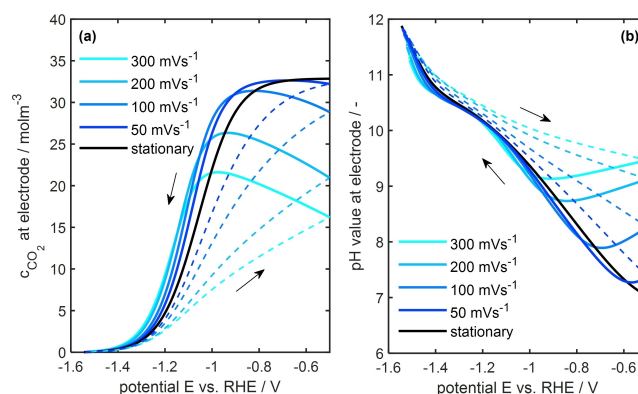


**Figure 2.** (a) Predicted CO<sub>2</sub> concentration at the electrode during the potential sweep for dynamic and steady-state simulation in dependency of the scan rate and (b) corresponding pH value at the electrode. Forward sweeps are shown in solid lines and backward sweep in dashed lines. Conditions: CO<sub>2</sub> saturated 0.1 M KHCO<sub>3</sub> solution, room temperature, rotation rate of 50 rpm.

whereas HER is not affected. The strong influence of the scan rate can be partly explained by the difference in the CO<sub>2</sub> concentration at the electrode (see Figure 2a): (1) At the upper potential of  $-0.5$  V, the CO<sub>2</sub> concentration decreases with increasing scan rate. (2) In the intermediate potential range of  $-0.5$  to  $-1.0$  V, the CO<sub>2</sub> concentrations during the potential sweep are significantly lower than for steady state and increases with decreasing potential for higher scan rates. (3) In all cases, CO<sub>2</sub> concentration drops to 0 in the low potential range of  $-1.0$  to  $-1.6$  V. This decline occurs earlier at slower scan rates. Additionally, the CO<sub>2</sub> concentration is much lower for the backward sweep than for the forward sweep at the same potential. The difference increases with scan rates, which explains the observed increasing current hysteresis with scan rate in Figure 1.

The curves for pH value at the electrode surface in Figure 2b show similar, but opposite trends compared to the CO<sub>2</sub> concentration as the scan rate changes. In the high potential region, pH values increase with increasing scan rate. In the

intermediate range, pH is reaching a plateau value which is the highest for the stationary case. With further decreasing potentials, pH increases nearly linearly again with highest values for stationary operation compared to dynamic operation. The pH value is a measure of hydrogen and CO<sub>2</sub> production, as OH<sup>-</sup> is produced in both reactions. In addition, OH<sup>-</sup> is consumed by carbonation in the electrolyte according to Equation (3)–(5). Therefore, most processes strongly change the pH near and at the electrode. The observed trend in the pH and CO<sub>2</sub> surface concentrations can be explained as follows:

- (1) The concentration differences in the upper potential region originate from the reaction history. For analysis of cyclic voltammograms, the 8<sup>th</sup> cycle is selected for accurate process analysis. It ensures that experimental and simulated current-potential curves are stable and reproducible regardless of the cycle number. However, this also means that the processes and state during the previous cycle influence the concentrations at the beginning of the next cycle. From about -0.8 V, the current of the backward sweep drops to almost zero, allowing more CO<sub>2</sub> to diffuse to the surface than is consumed. As a result, the CO<sub>2</sub> concentration at the electrode has time to recover during the backward sweep. This recovery time is longer for lower scan rates. For example, at -0.5 V, the CO<sub>2</sub> concentration for the sweep of 50 mVs<sup>-1</sup> is almost fully recovered and similar to that of the steady-state curve. In contrast, recovery time and thus CO<sub>2</sub> concentration decreases with increasing scan rate. Analogous to the CO<sub>2</sub> concentration, the pH is the highest for high scan rates, as OH<sup>-</sup> have not yet been transported away or reacted further to form carbonates. This effect also causes the hysteresis in current density, CO<sub>2</sub> reduction and the concentrations of CO<sub>2</sub> and hydroxide ions (pH) for the forward and backward sweep. Higher pH values and lower CO<sub>2</sub> concentrations during the backward sweep for higher scan rates reduce the current density.
- (2) The increase in CO<sub>2</sub> concentration with decreasing potential up to approx. -1 V for fast sweep rates is directly related to the recovery process. The diffusive transport of CO<sub>2</sub> from the bulk to the electrode and only small consumption rates of CO<sub>2</sub> causes the concentration to increase with time. Similarly, pH decreases due to the transport of OH<sup>-</sup> to the bulk and carbonation.
- (3) The smaller decline in CO<sub>2</sub> concentration in the low potential range with increasing scan rate is caused by the fact that the CO<sub>2</sub> consumption time in this potential range is much lower for higher scan rates. This results in higher CO<sub>2</sub> concentrations and a later depletion of CO<sub>2</sub> at the electrode during the sweep. It leads to a shift of the plateau value to higher absolute total current and higher absolute Faradaic current densities of CO<sub>2</sub>R. The pH increases earlier due to longer reaction time for lower scan rates. The stationary curve shows the highest pH value in this potential region. At a potential of around -1.3 V, a slight stagnation of the increase can be seen for all curves. This is due to the limitation of CO<sub>2</sub> reduction and the HER

becoming the dominant reaction, and corresponds to the plateau in current.

After the reversal point from forward to backward sweep, an increase in pH is observed, especially for high scan rates, although the current density decreases. This phenomenon will be discussed later in the section "Impact of carbonation reactions".

The observed behavior is not changed qualitatively with increasing electrolyte concentration of 0.5 or 1.0 M KHCO<sub>3</sub>, which is shown in Figure 12 of the Supporting Information.

Concluding, we have shown that the conditions at the electrode differ significantly between steady-state and dynamic operation. One reason for this is that the transport of CO<sub>2</sub> and OH<sup>-</sup> is slower than the potential change during the sweep for high scan rates. In addition, the reaction time, i. e., the time over which a potential is held, determines the extent of consumption and thus concentration change. This means that in cyclic voltammetry, species transport and carbonation impact on the measurements can be easily detected by varying the scan rate. A fast CV scan can only replace a steady state if there is no transport effect and no change in local conditions at the electrode. This is not possible for electrochemical CO<sub>2</sub> reduction under the investigated conditions. It has been shown that fast species transport has an essential impact at given conditions, so the influence of changing the hydrodynamic conditions will be investigated in the following.

### Impact of species transport

Adjusting a suitable diffusion layer thickness is essential for preventing transport limitations at planar electrodes in batch and flow cells. A thick layer will cause transport limitations leading to reduced reactant transport and thus reduced performance during stationary or dynamic operation. Consequently, the diffusion layer thickness strongly impacts the steady-state behavior and the dynamic response of the system to a change in current or – as here – in potential.

As shown in the previous section, variation in scan rate changes the impact that species transport through the diffusion layer has on performance and local concentrations at the electrode. This, in turn, means that changing the diffusion layer thickness should also lead to significant qualitative and quantitative changes in species transport and hence in performance. This finding will have practical implications for designing and adjusting cell configurations for CO<sub>2</sub>R.

For the investigation of transport effects, the impact of diffusion layer thicknesses was studied through variation of the rotation rate of the electrode between 50 to 300 rpm. Figure 3 shows the current densities during dynamic and stationary operation for 300 rpm. Current densities at a medium speed of 150 rpm are shown in Figure 8 in the Supporting Information. The current densities increase significantly with rotation rate from a maximum of -16 mA cm<sup>-2</sup> at 50 rpm to -27 mA cm<sup>-2</sup> at 300 rpm, when operating at -1.4 V. As expected, smaller diffusion layer thicknesses and faster species transport lead to significantly higher absolute current densities at intermediate

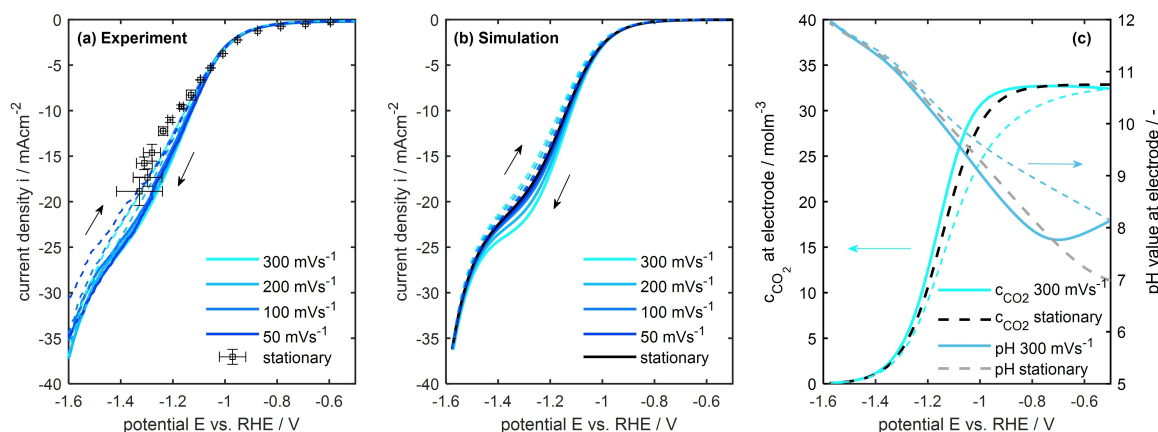


**Figure 3.** (a) Experimental and (b) simulated cyclic voltammograms for different scan rates and steady-state polarization curve for a rotation rate of 300 rpm ( $d = 45 \mu\text{m}$ ). (c) Predicted  $\text{CO}_2$  concentration at the electrode during the potential sweep for dynamic (scan rate of  $300 \text{ mVs}^{-1}$ ) and steady state simulation and corresponding pH value at the electrode. Forward sweeps are shown in solid lines and backward sweep in dashed lines. Conditions:  $\text{CO}_2$  saturated 0.1 M  $\text{KHCO}_3$  solution, room temperature. Potentials are corrected for  $iR$ -drop.

and low potentials. With more  $\text{CO}_2$  being available over a wide potential range, the limitation of  $\text{CO}_2\text{R}$  due to low  $\text{CO}_2$  concentrations at the electrode (see Figure 3c) is shifted to lower potentials, apparent in the shift of the current plateau in Figure 3b to more negative potentials and current densities.

The experimental and simulative results agree well, both show that the dependency of current on the scan rate and the difference between steady-state and dynamic currents, as well as the hysteresis during CV become smaller for higher rotation rates. At 300 rpm, there is almost no dependence on the scan rate. Thus, a small diffusion layer thickness allows to get similar results for steady-state and dynamic operation. Comparing the time constants of the diffusive transport  $\tau_{\text{diff}}$  with the time it takes for a potential sweep from  $-0.5 \text{ V}$  to  $-2.0 \text{ V}$  makes this dependence clear. The time constant can be calculated from Eq. (6)

$$\tau_{\text{diff}} \approx \frac{d^2}{D_{\text{CO}_2}} \quad (6)$$

with the diffusion layer thickness  $d$  and the diffusion coefficient of  $\text{CO}_2$   $D_{\text{CO}_2}$ . Increasing the rotation rate from 50 to 300 rpm decreases  $\tau_{\text{diff}}$  from 5.6 to 1.0 s. The time constant is now 5 times smaller than the time it takes for an unidirectional potential sweep of 5 s for a scan rate of  $300 \text{ mVs}^{-1}$ , whereas for 50 rpm, the times are similar. This means that at 300 rpm, sufficient  $\text{CO}_2$  can diffuse to the electrode and can partly be replenished during the sweeps. The  $\text{CO}_2$  concentration at the electrode is very similar for stationary and  $300 \text{ mVs}^{-1}$  operation, and there is no maximum anymore for 300 rpm. Also, the differences between steady-state and dynamic pH for a higher rotation has significantly decreased, amounting a pH difference at  $-0.5 \text{ V}$  of 1 for 300 rpm compared to a pH difference of 2.5 for 50 rpm.

Still, the pH recovery takes much longer and is not fully completed under the conditions shown here, as can be seen in the still visible pH minimum for dynamic operation. The readers should notice the logarithmic scale of pH, which emphasizes

differences in low absolute concentrations of hydroxide ions much more.

In comparison to 300 rpm, the results at 150 rpm, which corresponds to a diffusion layer thickness of  $50 \mu\text{m}$ , still has visible, although small hysteresis for the here investigated conditions of room temperature and 0.1 M  $\text{KHCO}_3$ , shown in Figure 8 of the SI. Thus, diffusion layer thicknesses  $\geq 45 \mu\text{m}$  lead to non-negligible differences in the dynamic and steady-state current response.

It is known from other simulative studies that the diffusion layer thickness in cell setups can vary in a wide range of 40 and  $200 \mu\text{m}$ .<sup>[24–25,40–41]</sup> Therefore, to see if the cell suffers from thick diffusion layers and thus transport losses, CVs can be used in the investigated cell setup at different scan rates. If they are equal, then there is no significant transport limitation. Besides increasing the electrolyte flow rate, the integration of turbulence promoters is possible to decrease the diffusion layer thickness in cells.

### Impact of carbonation reactions

The local pH is known to strongly influence the reaction conditions for  $\text{CO}_2$  reduction at the electrode.<sup>[40,42–43]</sup> Due to the production of  $\text{OH}^-$  during  $\text{CO}_2\text{R}$  and HER [Eq. (7)–(10)], the pH at the electrode increases, especially when high current densities are reached. The change in pH can be mitigated by the consumption of  $\text{OH}^-$  via the carbonation reaction with  $\text{CO}_2$  to form  $\text{CO}_3^{2-}$ , as given in Equation (4) and (5). Furthermore, molar transport of  $\text{OH}^-$  into the bulk may reduce the accumulation of  $\text{OH}^-$  at the surface, and thus a fast pH increase. It is still unclear how strong is the interaction of carbonation reactions and species transport, resulting in local pH change, and how it influences the stationary and dynamic behavior of the reaction system. In the following, we analyze this interplay and its effect on cell performance.

The changes in hydroxide ion concentration within the diffusion layer due to electrochemical and chemical reactions

and due to transport from bulk are shown for stationary operation in Figure 4a and for dynamic operation in Figure 4b. The main production of  $\text{OH}^-$  for both, stationary and dynamic operation, is due to the electrochemical reactions. It is equal to the current response, as both, HER and  $\text{CO}_2\text{R}$  produce one  $\text{OH}^-$  per  $\text{e}^-$ . It thus also increases with more negative potential. Most of these hydroxide ions are consumed by the chemical carbonation reactions (c1 and c2 in Figure 4). Their combined consumption curves resemble a mirror image of the electrochemical production rate. In contrast, the rates of hydroxide ions leaving the diffusion layer to the bulk or being produced or consumed by water dissociation are much lower; these  $\text{OH}^-$  sources/sinks are thus negligible. At potentials between  $-1.1$  V and  $-0.7$  V, the  $\text{CO}_2$ -to-bicarbonate reaction (c1) is slightly higher than the bicarbonate-to-carbonate reaction (c2) for stationary operation. This is caused by the good availability of  $\text{CO}_2$  in the diffusion layer for this potential range. For more negative potentials, the c1 reaction becomes slower than c2: Here,  $\text{CO}_2$  is depleted in the entire diffusion layer, and bicarbonate, which is produced by c1 and which is anyway present in the supplied electrolyte – can consume more of the ions.

For the dynamic operation, the situation changes. For the strongly negative potential region,  $\text{OH}^-$  consumption by c2 is much higher than for the c1 reaction. This is caused by the different time constants of these reactions. The c2 reaction is much faster due to a higher reaction rate constant and good availability of bicarbonate ions. This results in a domination of c2 reaction in dynamic operation and a large deviation from equilibrium concentrations of carbonate species. In the backward sweep after the reversal point, the consumption of hydroxide ions by c2 is decreasing strongly in the diffusion layer and becomes positive at a potential of  $-1.2$  V, so hydroxide ions are produced by c2. This effect is created by equilibration, i.e. the thrive to restore equilibrium concentrations of the carbonate system. At these conditions (referring to the local pH and  $\text{CO}_2$  concentration), the equilibrium predominantly favors

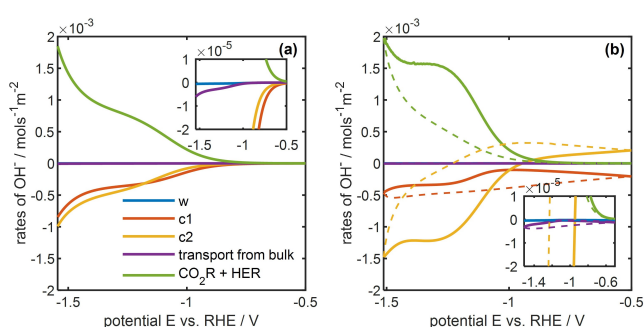


**Figure 4.** Molar transport or reaction rates of hydroxide ions in the diffusion layer caused by water dissociation (w), by  $\text{CO}_2$ -to-bicarbonate reaction (c1) and by bicarbonate-to-carbonate reaction (c2), by transport of hydroxide ions from the bulk and by the electrochemical reactions HER and  $\text{CO}_2\text{R}$  for a rotation rate of 50 rpm for (a) stationary and (b) dynamic operation. Forward sweeps at  $300\text{ mVs}^{-1}$  are shown in solid lines and backward sweep in dashed lines. Conditions:  $\text{CO}_2$  saturated 0.1 M  $\text{KHCO}_3$  solution, rotation rate of 50 rpm, room temperature. Potentials are corrected for iR-drop.

the formation of bicarbonate ions, so carbonate ions react to bicarbonate, and  $\text{CO}_2$  reacts with released  $\text{OH}^-$  to bicarbonate.

In summary, due to a good availability of bicarbonate and a fast bicarbonate-carbonate buffer reaction, bicarbonate consumes most of the  $\text{OH}^-$  at low potentials, whereas it releases them at higher potentials again, when less  $\text{OH}^-$  are produced in dynamic operation.

Figure 5 compares the ratio of the total electrochemical  $\text{CO}_2$  consumption to the chemical  $\text{CO}_2$  consumption over the entire diffusion layer thickness. The absolute values of the consumption rates can be found in Figure 11 of the Supporting Information. The ratio of the  $\text{CO}_2$  consumption rates is in the order of 1, i.e., chemical and electrochemical consumption are in the same order of magnitude. All values are further positive, which means that there is no release or source of  $\text{CO}_2$  from decarbonisation of the  $\text{KHCO}_3$  electrolyte. This effect has also been observed in gas diffusion electrodes<sup>[44]</sup> and is acutely exacerbated in planar electrodes due to low  $\text{CO}_2$  concentrations. For the stationary case, in the high potential region  $> -1$  V, the ratio of  $\text{CO}_2$  consumption is slightly less than 1 and nearly constant. In this potential region, the reaction rate of  $\text{CO}_2\text{R}$  is low and chemical  $\text{CO}_2$  consumption takes place for consuming these hydroxide ions from  $\text{CO}_2\text{R}$  and HER. With decreasing potential, the ratio reaches a maximum of 1 at a potential of  $-1.3$  V. At this potential, the electrochemical  $\text{CO}_2$  reduction has its maximum, and the ratio of 1 indicates that for each  $\text{CO}$  molecule produced, two  $\text{CO}_2$  molecules are converted in the diffusion layer – one by electrochemical reduction and one by chemical reaction with a hydroxide ion. At low potentials, the ratio decreases further due to the limitation of  $\text{CO}_2$  reduction and HER dominance. In this potential range,  $\text{CO}_2$  is mainly consumed by the chemical reaction using the hydroxide ions released by HER, which further suppresses the electrochemical  $\text{CO}_2\text{R}$ .

The situation under dynamic operation is significantly different compared to stationary operation. For the forward sweep, electrochemical consumption exceeds that of chemical consumption in the medium potential range. Here, the Faradaic

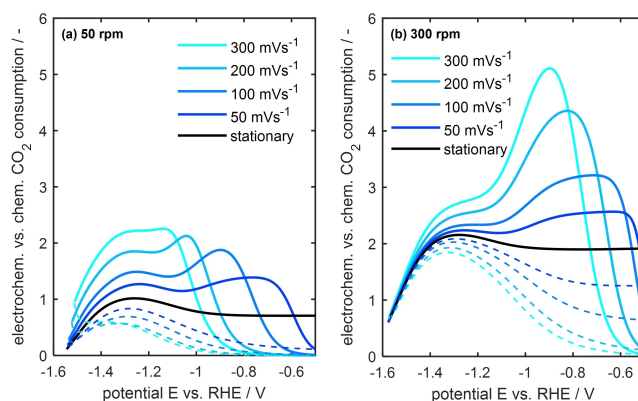


**Figure 5.** Ratio of electrochemical  $\text{CO}_2$  consumption to chemical  $\text{CO}_2$  consumption in the diffusion layer along the potential for steady-state and for dynamic operation at different scan rates for (a) 50 rpm and (b) 300 rpm. Forward sweeps are shown in solid lines and backward sweep in dashed lines. Conditions:  $\text{CO}_2$  saturated 0.1 M  $\text{KHCO}_3$  solution, room temperature. Potentials are corrected for iR-drop.

current of the CO<sub>2</sub>R is strong as most of the OH<sup>-</sup> ions are more rapidly consumed by the bicarbonate-to-carbonate reaction than the CO<sub>2</sub>-to-bicarbonate reaction (see discussion above). The chemical consumption exceeds electrochemical reaction for very negative potentials – similarly as for the stationary case – due to high HER and thus hydroxide production, which consumes fresh CO<sub>2</sub> entering the diffusion layer.

During the backward sweep, this accumulation of OH<sup>-</sup> leads to high carbonation rates, thus the ratio drops to almost zero. This history and the ongoing balancing of the buffer also explains the very low ratios of electrochemical vs. chemical CO<sub>2</sub> consumption at the beginning of the forward sweep. At low potentials < -1.4 V, the consumption ratio decreases and continues to decrease further in the backward sweep at high scan rates, resulting in a significant hysteresis. The reason for the hysteresis effect is the readjustment of the carbonate equilibrium. This results in low values of the consumption ratio of CO<sub>2</sub> for the backward sweep and a strong hysteresis in dynamic operation.

Interestingly, electrochemical CO<sub>2</sub> reduction is significantly more favored than carbonation when increasing rotation to 300 rpm, as shown in Figure 5b. The ratio is also higher for steady state, with a value of about 2. This is because the buffering is mainly done by the bicarbonate-to-carbonate reaction in this case. A thinner diffusion layer ensures high availability of bicarbonate ions and low concentrations of carbonate species which promotes high reaction rates of reaction c2 (see Figure 9 in SI). For dynamic operation, the potential range where chemical CO<sub>2</sub> consumption is higher than the electrochemical one becomes smaller because the diffusion layer recovers much faster. For scans at 50 mV s<sup>-1</sup>, during the full scan, electrochemical CO<sub>2</sub> consumption is higher than chemical one. In addition, for all scan rates, the maximum is shifted to more positive potentials. At high potentials, the CO<sub>2</sub> reduction is not transport limited, and due to better transport, the local pH is not high, which prevents carbonation. These points favor strongly the electrochemical CO<sub>2</sub> reduction over the chemical consumption. Thus, either at low potentials, where high current densities can be achieved, higher values of the consumption ratio are reached due to better species transport.

We conclude that with higher scan and rotation rates, the selectivity of the CO<sub>2</sub> consumption can be pushed in favor of electrochemical CO<sub>2</sub> reduction. This can be reached due to a better transport of CO<sub>2</sub> and bicarbonate species and a fast reaction rate of bicarbonate-to-carbonate reaction.

### Faradaic efficiency

In the following, we discuss the practical impact of the complex influence of carbonation and species transport on electrochemical CO<sub>2</sub> reduction. We focus on impact on catalyst characterization and performance assessment. Questions answered are whether dynamic operation or operation at thin vs. thick diffusion layers should be targeted.

The Faradaic efficiency characterizes the selectivity for the electrochemical CO<sub>2</sub>R over HER. Figure 6 shows the simulated Faradaic efficiencies for 50 rpm and 300 rpm in stationary and dynamic operation. At high potentials, in all cases, high  $FE_{CO_2R}$  near to 1 is reached for dynamic and stationary operation at low and higher rotation rates. This is maintained by high CO<sub>2</sub> concentrations and low reaction rates. At lower potentials, the Faradaic efficiencies decrease due to the transport-controlled limitation of CO<sub>2</sub>R and the strong onset of HER. For low rotation rates and low potentials below -1.4 V, the Faradic efficiency is higher for the dynamic vs. stationary operation. For dynamic operation at -1.4 V (forward sweep), it is 10% higher. This is due to the slower depletion of CO<sub>2</sub> at the electrode, slightly lower pH values, and a higher selectivity of electrochemical over chemical CO<sub>2</sub> consumption. The  $FE_{CO_2R}$  in the backward sweep is slightly lower than that for stationary operation, caused by higher pH values shifting the CO<sub>2</sub> consumption towards chemical consumption. This results in lower CO<sub>2</sub> concentrations at higher potentials in the backward sweep. Increasing the rotation rate to 300 rpm further increases the  $FE_{CO_2R}$ . Improving the species transport increases the local CO<sub>2</sub> concentration and the selectivity of CO<sub>2</sub> consumption towards electrochemical consumption. However, at this rotation rate, the  $FE_{CO_2R}$  for the dynamic and stationary analyses are almost the same. The differences in local conditions in this potential region are minor, and the transport processes are faster than the potential sweep. This reduces the impact of the scan rate and is reflected in very similar Faradaic efficiencies.

These observations show that the differences in the local state between the dynamic and the stationary operation result in a significant shift in the Faradic efficiency, if species transport is insufficient. It shows, that from catalyst material characterisation with high rotation rates no conclusion for performance under mass transport influence can be made. For systems without transport limitation, dynamic characterization can be

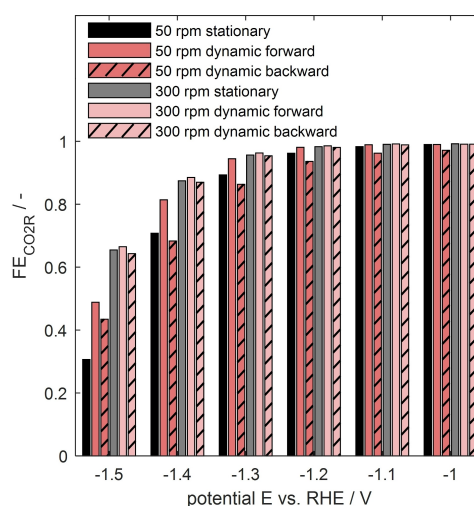


**Figure 6.** Simulated Faradaic efficiencies of electrochemical CO<sub>2</sub> reduction for stationary and dynamic operation for 50 and 300 rpm. Values for forward sweeps at 300 mV s<sup>-1</sup> are shown without pattern and values for backward sweep with striped pattern. Conditions: CO<sub>2</sub> saturated 0.1 M KHCO<sub>3</sub> solution, room temperature. Potentials are corrected for iR-drop.

used to infer steady-state performance. Additionally, we showed, if species transport effects cannot be excluded, dynamic operation can help to shift the  $FE_{\text{CO}_2\text{R}}$  to higher values. The improvement is strongly dependent on the time constants of transport processes compared to time constants of the potential sweep and is only a snap-shot of performance. The performance under steady-state conditions can differ significantly from this. Whether a permanent improvement of performance can be made with dynamic operation techniques, has to be investigated in further studies.

## Conclusions

This work used a dynamic model for electrochemical  $\text{CO}_2$  reduction at silver electrodes to analyze the difference between steady-state and transient behavior systematically, and to unravel the impact of transport and carbonation on the performance of the silver electrode. The model was able to reproduce polarization curves and cyclic voltammograms with different scan rates and rotation rates, i.e. species transport influences. A high scan rate dependence on the current response was observed for low rotation rates. Such conditions can easily occur under real operating conditions, e.g. in flow cell setups. This sensitivity to scan rate results from species transport affecting several aspects of the system, namely  $\text{CO}_2$  depletion, carbonate buffer reaction, and local pH evolution.

Under transport limitation, stationary operation suffers most from depletion of  $\text{CO}_2$  at the electrode due to slow transport and increased chemical consumption of  $\text{CO}_2$  by carbonation reaction. Applying high scan rates, Faradaic efficiency for  $\text{CO}_2\text{R}$  can be increased for the forward sweep. This is reached due to several effects: The holding times at low potential is much shorter and the  $\text{CO}_2$  concentration at the electrode surface partially recovered by species transport during the backward sweep in dynamic operation. Thus, the concentration profile across the diffusion layer is mainly influenced by the reaction history and the scan rate. Additionally, it is shown that the effect of carbonation is highly time dependent. The reaction  $\text{HCO}_3^- + \text{OH}^- \rightleftharpoons \text{CO}_3^{2-} + \text{H}_2\text{O}$  is much faster than the reaction  $\text{CO}_2 + \text{OH}^- \rightleftharpoons \text{HCO}_3^-$  due to good availability of bicarbonate compared to  $\text{CO}_2$  in the electrolyte and a higher reaction rate constant of the former reaction. This results in a domination of this reaction in the buffer process and less consumption of  $\text{CO}_2$  by the chemical reaction in dynamic operation. The selectivity of  $\text{CO}_2$  consumption by electrochemical vs. buffer reaction is increased more than two-fold by increasing the rotation rate from 50 to 300 rpm. This is caused by better  $\text{CO}_2$  transport to the electrode, a better transport of bicarbonate and carbonate ions which promotes the bicarbonate-to-carbonate reaction in the diffusion layer.

As species transport and carbonation effects can be easily detected by varying the scan rate, we propose such a test for catalyst research to assure that the results contain negligible transport effect. Transport effects can easily be removed by increasing rotation rates in RDE setups. In contrast, when it is of interest to understand how the catalyst behaves during realistic

conditions, where carbonation and species transport will lead to strongly different pH and local concentrations, the proposed low rotation rates and a variation in scan rate can be applied. We recommend to replace steady-state analysis with the dynamic analysis for RDE studies- with choice of the appropriate rotation rate – because it is faster and less prone to failure in gas evolution reactions. Concluding, the  $\text{CO}_2$  reduction in alkaline electrolyte has been shown as a system where electrolyte conditions may easily change and deviate from nominal conditions; these in turn can strongly impact performance and analysis results. This requires countermeasures as suggested here for adjusting proper analysis conditions.

## Methods

### Experimental characterization

All electrochemical measurements were conducted in a three-electrode setup using a PTFE cell with an electrolyte volume of 250 mL. As a working electrode, a planar silver rotating disk electrode (surface area  $A_{\text{geom}} = 0.1963 \text{ cm}^2$ ) with PEEK shroud from PINE Research Instrumentation Inc., and as counter electrode, a spiral platinum wire was used. All potentials were measured and plotted against a reference electrode, the HydroFlex reversible hydrogen electrode (RHE) from Gaskatel mbH. The potentials were corrected for uncompensated resistance afterward. For variation of rotation rates, a rotating disk electrode setup from PINE Research Instrumentation Inc. was connected with a Gamry Interface 1010E potentiostat. Before each measurement, the silver electrode was polished with diamond compound with a particle size of  $0.25 \mu\text{m}$  from Kemet. As a solvent and for rinsing, deionized water ( $16 \text{ M}\Omega\text{cm}$ ) was used. Aqueous potassium bicarbonate solution ( $0.1 \text{ M}$ , BioUltra  $\geq 99.5\%$ , Sigma Aldrich) was used as electrolyte. The electrolyte was purged with  $\text{CO}_2$  for 15 min before starting the experiment to ensure saturation with  $\text{CO}_2$ . During the experiment, a  $\text{CO}_2$  atmosphere was realized in the gas volume above the solution.

Cyclic voltammetry was performed in a potential window of  $-0.5$  to  $-2.0 \text{ V}$  vs. RHE with rotation speeds between 50 and 150 rpm and between  $-0.5$  to  $-2.5 \text{ V}$  vs. RHE for 300 rpm. The scan rate of the potential sweep was set to values of  $\nu = \{50; 100; 200; 300 \text{ mV s}^{-1}\}$ . The number of cycles was eight for each scan rate to guarantee a quasi-steady state. In the figures, only the last cycle is displayed.

Electrochemical impedance spectra were recorded for each scan rate after a CV measurement. It was used to determine the uncompensated resistance for iR-drop correction of the reference electrode potential. Therefore, an AC voltage amplitude of  $10 \text{ mV}_{\text{rms}}$  was applied at an underlying DC voltage of  $-0.5 \text{ V}$  vs. RHE in a frequency range between 1 MHz and 1 Hz.

The stationary polarisation curve was measured by holding a constant potential for 200 s. The step size of the applied potential was  $0.1 \text{ V}$ . It was observed that the current density was decreasing with time for measured current densities above  $10 \text{ mAcm}^{-2}$ . This was induced by the bubble accumulation at the electrode and resulted in the increase of the uncompensated resistance with time. The uncompensated resistance was measured after each holding time. Figures show the corrected mean potential and mean error, determined from the last 20 s of each measured potential. Due to the bubble formation, the minimal applied potential of the polarization curve was limited to values around  $-1.3 \text{ V}$  vs. RHE at rotation rates of 150 and 300 rpm.

## Dynamic macrokinetic modelling approach

Table 1. Model parameters.

Parameter	Symbol	Value	Unit	Source
Operation conditions				
Concentration of electrolyte	$c_{\text{elyt}}$	0.1	mol L <sup>-1</sup>	
Pressure of gas side for CO <sub>2</sub>	$p_{\text{CO}_2}$	1	atm	
Temperature	$T$	298.15	K	assumed
Geometrical surface area of electrode	$A_{\text{geom}}$	$1.9635 \cdot 10^{-5}$	m <sup>2</sup>	
Internal ohmic resistance	$R_{\text{int}}$	130	$\Omega$	measured
Diffusion layer thickness for a rotation rate of 50 rpm	$d_{50 \text{ rpm}}$	$103.0 \cdot 10^{-6}$	m	estimated <sup>1</sup>
Diffusion layer thickness for a rotation rate of 150 rpm	$d_{150 \text{ rpm}}$	$50.3 \cdot 10^{-6}$	m	estimated <sup>1</sup>
Diffusion layer thickness for a rotation rate of 300 rpm	$d_{300 \text{ rpm}}$	$44.7 \cdot 10^{-6}$	m	estimated <sup>1</sup>
Electrochemical surface reaction				
Reaction rate constant for forward reaction of electrochemical CO <sub>2</sub> adsorption	$k_{0,f,1}$	$8.076 \cdot 10^{-6}$	mol m <sup>-2</sup> s <sup>-1</sup>	optimized
Reaction rate constant for forward reaction of electrochemical CO desorption	$k_{0,f,2}$	$7.708 \cdot 10^{-4}$	mol m <sup>-2</sup> s <sup>-1</sup>	optimized
Reaction rate constant for forward reaction of electrochemical H <sub>2</sub> O adsorption (Volmer step)	$k_{0,f,3}$	$7.550 \cdot 10^{-10}$	mol m <sup>-2</sup> s <sup>-1</sup>	optimized
Reaction rate constant for forward reaction of electrochemical H <sub>2</sub> desorption (Heyrovsky step)	$k_{0,f,4}$	$8.532 \cdot 10^{-8}$	mol m <sup>-2</sup> s <sup>-1</sup>	optimized
Charge transfer coefficient for CO <sub>2</sub> reduction	$\alpha_{\text{CO}_2\text{R}}$	0.661	–	optimized
Charge transfer coefficient for hydrogen evolution reaction	$\alpha_{\text{HER}}$	0.687	–	optimized
Standard redox potential of CO <sub>2</sub> R	$E_{\text{CO}_2\text{R}}^{\text{00}}$	-0.11	V	[46]
Standard redox potential of HER	$E_{\text{HER}}^{\text{00}}$	0	V	[46]
Specific capacitance of electrochemical double layer	$C_{\text{DL}}$	100	$\mu\text{F cm}^{-2}$	measured
Concentration of surface adsorption sites	$\Gamma$	$7.04 \cdot 10^{-6}$	mol m <sup>-2</sup>	[46]
Electrolyte conditions				
Activity coefficient of dissolved species $j$	$\gamma_j$	1	–	assumed
Standard concentration of dissolved species $j$	$c_j^{\ominus}$	1	kmol m <sup>-3</sup>	assumed
Diffusion coefficient of dissolved CO <sub>2</sub>	$D_{\text{CO}_2}$	$1.91 \cdot 10^{-9}$	m <sup>2</sup> s <sup>-1</sup>	[47]
Diffusion coefficient of H <sub>2</sub> O	$D_{\text{H}_2\text{O}}$	$2.57 \cdot 10^{-9}$	m <sup>2</sup> s <sup>-1</sup>	[48]
Diffusion coefficient of OH <sup>-</sup>	$D_{\text{OH}^-}$	$5.273 \cdot 10^{-9}$	m <sup>2</sup> s <sup>-1</sup>	[49]
Diffusion coefficient of H <sup>+</sup>	$D_{\text{H}^+}$	$9.311 \cdot 10^{-9}$	m <sup>2</sup> s <sup>-1</sup>	[49]
Diffusion coefficient of HCO <sub>3</sub> <sup>-</sup>	$D_{\text{HCO}_3^-}$	$1.185 \cdot 10^{-9}$	m <sup>2</sup> s <sup>-1</sup>	[49]
Diffusion coefficient of CO <sub>3</sub> <sup>2-</sup>	$D_{\text{CO}_3^{2-}}$	$0.923 \cdot 10^{-9}$	m <sup>2</sup> s <sup>-1</sup>	[49]
Diffusion coefficient of K <sup>+</sup>	$D_{\text{K}^+}$	$1.957 \cdot 10^{-9}$	m <sup>2</sup> s <sup>-1</sup>	[49]

<sup>1</sup> estimated close to Levich equation (see Supporting Information).

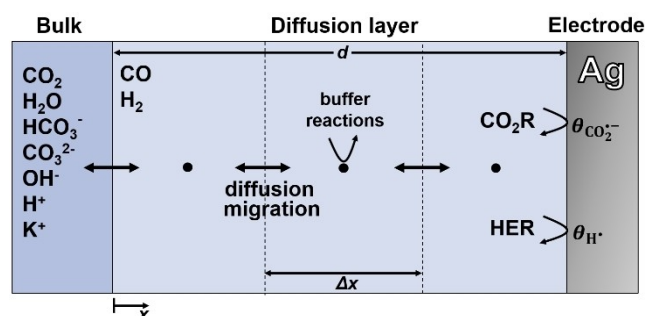
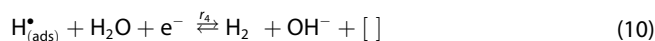
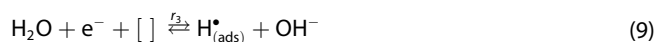


Figure 7. Model representation for the CO<sub>2</sub>R at planar silver electrode with all involved species, transport mechanisms in the diffusion layer, carbonatization and competing hydrogen evolution reaction (HER).

In this section, the mathematical model is presented, and a detailed explanation of the individual model equations and underlying assumptions is given. All constant model parameters can be found in Table 1.

The model includes the description of a planar silver electrode, as well as the diffusion layer in front of the electrode and the adjacent bulk electrolyte phase (see Figure 7). The concentration of the bulk electrolyte is assumed to be constant due to its large electrolyte volume and the low total CO<sub>2</sub> consumption relative to its overall concentration in the bulk solution. The bulk concentrations are used as boundary conditions for the model at the interface between diffusion layer and bulk. The electrochemical reaction system is assumed as a two-step mechanism for the CO<sub>2</sub>R and the

alkaline HER, respectively.<sup>[45]</sup> The latter is described by the Volmer-Heyrovsky mechanism. This leads to the following reaction equations and allows the description of competitive adsorption and surface blockage [Eq. (7)–(10)].



[ ] denotes a free catalyst surface site. The surface specific electrochemical reaction rate  $r_i$  of each surface reaction  $i$  is calculated by a Butler-Volmer-equation approach following Eq. (11)–(14)

$$r_1 = k_{0,f,1} \cdot \exp\left(\frac{-(1 - \alpha_{\text{CO}_2\text{R}})F}{RT} \cdot \eta_1\right) \cdot a_{\text{surf,CO}_2} \cdot \theta_{[\ ]} - k_{0,b,1} \cdot \exp\left(\frac{\alpha_{\text{CO}_2\text{R}}F}{RT} \cdot \eta_1\right) \cdot \theta_{\text{CO}_2^*} \quad (11)$$

$$r_2 = k_{0,f,2} \cdot \exp\left(\frac{-(1 - \alpha_{\text{CO}_2\text{R}})F}{RT} \cdot \eta_2\right) \cdot \theta_{\text{CO}_2^*} \cdot a_{\text{surf,H}_2\text{O}} - k_{0,b,2} \cdot \exp\left(\frac{\alpha_{\text{CO}_2\text{R}}F}{RT} \cdot \eta_2\right) \cdot a_{\text{surf,CO}} \cdot a_{\text{surf,OH}^-}^2 \cdot \theta_{[\ ]} \quad (12)$$

$$r_3 = k_{0,f,3} \cdot \exp\left(\frac{-(1 - \alpha_{\text{HER}})F}{RT} \cdot \eta_3\right) \cdot a_{\text{surf,H}_2\text{O}} \cdot \theta_{[\ ]} - k_{0,b,3} \cdot \exp\left(\frac{\alpha_{\text{HER}}F}{RT} \cdot \eta_3\right) \cdot \theta_{\text{H}^*} \cdot a_{\text{surf,OH}^-} \quad (13)$$

$$r_4 = k_{0,f,4} \cdot \exp\left(\frac{-(1 - \alpha_{\text{HER}})F}{RT} \cdot \eta_4\right) \cdot a_{\text{surf,H}_2\text{O}} \cdot \theta_{\text{H}^*} - k_{0,b,4} \cdot \exp\left(\frac{\alpha_{\text{HER}}F}{RT} \cdot \eta_4\right) \cdot a_{\text{surf,H}_2} \cdot a_{\text{surf,OH}^-} \cdot \theta_{[\ ]} \quad (14)$$

with  $k_{0,i}$  being the reaction rate constants of forward (f) and backward (b) reaction  $i$ , the overpotential  $\eta_i$ ,  $\alpha$  the anodic charge transfer coefficient of  $\text{CO}_2\text{R}$  or HER, the activity of dissolved species  $a_{\text{surf},j}$  with  $j \in \Omega = \{\text{CO}_2; \text{CO}; \text{OH}^-; \text{H}_2; \text{H}_2\text{O}; \text{HCO}_3^-; \text{CO}_3^{2-}; \text{H}^+; \text{K}^+\}$  at the catalyst surface and coverage of adsorbed species and free adsorption sites  $\theta_k$  with  $k \in \Omega = \{\text{CO}_2^*(\text{ads}); \text{H}^*(\text{ads}); \text{free adsorption sites } [\ ]\}$ . The backward reaction rate constants turned out to be insensitive in the simulated potential range because the investigated potential range is far away from open circuit potential and anodic potential range. Hence, the values of backward reaction rate constants  $k_{0,b,i}$  were set to a value of  $10^{-25} \text{ mol m}^{-2} \text{ s}^{-1}$ .

The activities of dissolved species were calculated assuming ideal behavior of a diluted solution. Thus, we set activity coefficient to  $\gamma_j = 1$  and standard concentration to  $c_j^\ominus = 1 \text{ kmol m}^{-3}$  [Eq. (15)].

$$a_j = \gamma_j \frac{c_j}{c_j^\ominus} \quad (15)$$

The activity of water as a solvent is set to  $a_{\text{H}_2\text{O}} = 1$ . And the activity and concentration of dissolved product gases CO and  $\text{H}_2$  were neglected due to their low solubility in water.

The shift of the overpotential  $\eta$  due to pH using RHE reference electrode is calculated via Nernst equation [Eq. (16)]:

$$\eta_i = E - (E_i^{00} - 2.303 \frac{RT}{F} \cdot \text{pH}_{\text{bulk}}) \quad (16)$$

with  $E_i^{00}$  as the standard potential of reaction  $i$ .  $E_i^{00}$  are set equal for single steps of  $\text{CO}_2$  reduction with  $E_{\text{CO}_2\text{R}}^{00}$  and for HER to  $E_{\text{HER}}^{00}$  as it is done for lumped reaction kinetics.<sup>[46]</sup> Differences in  $E_i^{00}$  or free energies of reaction  $\Delta G_i$  are included in the reaction rate constants.

The electrochemical double layer is related to a potential drop at the electrode to electrolyte boundary. It is not locally resolved. Thus, the charge balance results in [Eq. (17)]

$$\frac{dE}{dt} = \frac{1}{C_{\text{DL}}} (i - F \sum_i r_i) \quad (17)$$

where  $C_{\text{DL}}$  is the specific electrochemical double layer capacitance of the electrode and  $i$  the total current. The electrode potential is calculated by correcting the external potential  $E_{\text{ext}}$ , which is the measured potential vs. RHE, with the potential drop due to uncompensated resistance with the current density  $i$ , the geometrical surface of the electrode  $A_{\text{geom}}$  and the internal resistance  $R_{\text{int}}$  [Eq. (18)]:

$$E = E_{\text{ext}} - i A_{\text{geom}} R_{\text{int}} \quad (18)$$

Molar transport fluxes  $N$  of all dissolved species  $j$  are described by the Nernst-Planck equation with Fick diffusion and migration [Eq. (19)]:

$$N_j = -D_j \nabla c_j - z_j u_j F c_j \nabla \phi \quad (19)$$

with  $z_j$  being the charge number of species  $j$  and  $\nabla \phi$  the potential gradient in the electrolyte phase. The mobility of the species  $u_j$  is approximated with the Nernst-Einstein equation for diluted systems by using the diffusion coefficient  $D_j$  [Eq. (20)]:

$$u_j = \frac{D_j}{RT} \quad (20)$$

The charge transfer between both electrodes, i.e. the current density in the electrolyte phase is given by Eq. (21):

$$i = F \sum_j z_j N_j \quad (21)$$

As a closing condition, to establish electroneutrality, conservation of this ionic current with no divergence in the electrolyte is assumed

$$\nabla i = 0 \quad (22)$$

Combining Equation (19) with Equation (21) results in

$$-\sigma \nabla \phi = i + F \sum_j z_j D_j \nabla c_j \quad (23)$$

where  $\sigma(x)$  is the local ionic conductivity of the electrolyte phase described by Eq. (24).

$$\sigma(x) = \sum_j \frac{z_j^2 F^2 D_j}{RT} c_j(x). \quad (24)$$

Equation (23) is used to calculate  $\nabla\phi$ .

Applying conservation of mass, the adsorbed species at the surface can be balanced as [Eq. (25)]

$$\frac{\partial\theta_k}{\partial t} = \frac{1}{\Gamma} \sum_i \nu_{j,i} r_{A,i} \quad (25)$$

where  $\theta_k$  is the surface coverage of the adsorbed species  $k$  and  $\Gamma$  is the concentration of surface adsorption sites at the catalyst surface.

For the species in the electrolyte, the respective species balance is [Eq. (26)]:

$$\frac{\partial c_j}{\partial t} = -\nabla N_j + \dot{S}_j. \quad (26)$$

$\dot{S}_j$  is the source term of species  $j$  in the electrolyte due to consumption or production in reactions at the electrode surface  $K$  and homogeneous chemical reactions in the electrolyte  $L$ , where species  $j$  is consumed or produced [Eq. (27)].

$$\dot{S}_j = \sum_{i=1}^K \frac{\nu_{j,i} r_i}{\Delta x} + \sum_{i=1}^L \nu_{j,i} r_i \quad (27)$$

with  $\Delta x$  as the width of the volume element next to the electrode. To account for carbonation or decarbonation reactions occurring in the electrolyte, the homogenous, chemical reaction in the electrolyte phase under alkaline and neutral conditions are considered [Eq. (3)–(5)].<sup>[50–51]</sup>

The values of the forward reaction rate constants  $k_{f,i}$  and equilibrium constants  $K_i$  are shown in Table 2 for electrolyte concentration of 0.1 M KHCO<sub>3</sub>. The backward reaction rate constants  $k_{b,i}$  are calculated by [Eq. (28)]

$$K_i = \frac{k_{i,f}}{k_{i,b}}. \quad (28)$$

The volumetric chemical reaction rates for water dissociation (w), CO<sub>2</sub> carbonation (c1) and HCO<sub>3</sub><sup>-</sup> carbonation (c2) are thus given by [Eq. (29–31)]:

$$r_w = k_{f,w} - k_{b,w} \cdot c_{H^+} \cdot c_{OH^-} \quad (29)$$

$$r_{c1} = k_{f,c1} \cdot c_{CO_2} \cdot c_{OH^-} - k_{b,c1} \cdot c_{HCO_3^-} \quad (30)$$

$$r_{c2} = k_{f,c2} \cdot c_{HCO_3^-} \cdot c_{OH^-} - k_{b,c2} \cdot c_{CO_3^{2-}} \quad (31)$$

This takes into account that the ionic species of the carbonate reaction system are not necessarily in equilibrium.

The concentration of dissolved CO<sub>2</sub>  $c_{CO_2(diss)}$  is calculated by Henry's law [Eq. (32)]:

$$c_{CO_2(diss)}^0 = H_{CO_2}^{CP} \cdot p_{CO_2} \quad (32)$$

with the Henry coefficient  $H_{CO_2}^{CP}$  and CO<sub>2</sub> partial pressure  $p_{CO_2}$ . The partial pressure is assumed as 1 atm. The Henry coefficient  $H_{CO_2}^{CP}$  for pure water depending on temperature is calculated by Equation (33) assuming isothermal condition with a temperature of 298.15 K [Eq. (33)].

$$\ln H_{CO_2}^{CP} = 93.4517 \cdot \left(\frac{100}{T}\right) - 60.2409 + 23.3585 \cdot \ln\left(\frac{T}{100}\right) \quad (33)$$

The decrease of solubility with increasing salt concentration in the electrolyte by the "salting-out" effect is considered by Sechenov equation [Eq. (34)].<sup>[52]</sup>

$$\log\left(\frac{c_{CO_2(diss)}^0}{c_{CO_2(diss)}}\right) = \sum_m (h_{CO_2} + h_m) c_m \quad (34)$$

It requires the consideration of all dissolved ionic species  $m \in \Omega = \{OH^-; HCO_3^-; CO_3^{2-}; H^+; K^+\}$  by their substance specific parameter  $h_m$  and their concentrations  $c_m$ . The values of parameters can be found in Table 3. Thus, the concentration of dissolved CO<sub>2</sub> in pure water  $c_{CO_2(diss)}^0$  is corrected to yield the concentration of dissolved CO<sub>2</sub> in electrolyte solution  $c_{CO_2(diss)}$  which is used in the model.

The model was implemented in MATLAB R2020b, and differential equations were solved with ode15s solver. Spatial discretization was done with an equidistant grid and applying finite volume method and central differential quotients. Grid size was set to a value of  $\Delta x = 1 \mu\text{m}$  and convergence of the solution regarding grid parameters was confirmed as refining the parameters lead to no visual changes of the CVs and concentration profiles. The system was initialized by holding the starting potential of  $-0.5 \text{ V}$ , where no significant electrochemical reactions take place, until a stationary state was reached. Initial surface coverages  $\theta_{k,t=0}$  and  $E_{t=0}$  were adapted from the stationary state. Initial concentrations were set to

**Table 2.** Values of reaction rate constants and equilibrium constants for the carbonate reaction system for a concentration of 0.1 M KHCO<sub>3</sub> and T = 298.15 K.

Parameter	Value	Unit	Source
$k_{f,w}$	$2.4 \cdot 10^{-2}$	$\text{mol m}^{-3} \text{s}^{-1}$	[50]
$K_w$	$1 \cdot 10^{-8}$	$\text{mol}^2 \text{m}^{-6}$	[51]
$k_{f,c1}$	5.93	$\text{m}^3 \text{mol}^{-1} \text{s}^{-1}$	[50]
$K_{c1}$	$4.44 \cdot 10^4$	$\text{m}^3 \text{mol}^{-1}$	[51]
$k_{f,c2}$	$1 \cdot 10^5$	$\text{m}^3 \text{mol}^{-1} \text{s}^{-1}$	[50]
$K_{c2}$	4.66	$\text{m}^3 \text{mol}^{-1}$	[51]

**Table 3.** Model parameters for the consideration of "salting-out" effect for the solubility of CO<sub>2</sub> in ionic solutions.

Constant	Value	Unit	Source
$h_{CO_2,0}$	-0.0172	$\text{m}^3 \text{kmol}^{-1}$	[52]
$h_{T,CO_2}$	-0.000338	$\text{m}^3 \text{kmol}^{-1} \text{K}^{-1}$	[52]
$h_{H^+}$	0	$\text{m}^3 \text{kmol}^{-1}$	[52]
$h_{K^+}$	0.0922	$\text{m}^3 \text{kmol}^{-1}$	[52]
$h_{OH^-}$	0.0839	$\text{m}^3 \text{kmol}^{-1}$	[52]
$h_{HCO_3^-}$	0.0967	$\text{m}^3 \text{kmol}^{-1}$	[52]
$h_{CO_3^{2-}}$	0.1423	$\text{m}^3 \text{kmol}^{-1}$	[52]

electrolyte bulk concentrations, where equilibrium of carbonate species and dissolved CO<sub>2</sub> is adjusted.

The reaction rate constants for the forward reaction of the electrochemical reactions  $k_{0,f,1}$ ,  $k_{0,f,2}$ ,  $k_{0,f,3}$ ,  $k_{0,f,4}$  and the charge transfer coefficient of CO<sub>2</sub>R  $\alpha_{\text{CO}_2\text{R}}$  and HER  $\alpha_{\text{HER}}$  were identified by optimizing the model output on experimental CV curves for the scan rates of 50 and 200 mV s<sup>-1</sup> at a rotation rate of 50 rpm. For higher rotation rates of 150 and 300 rpm, only the diffusion layer thickness was adapted. The kinetic parameters were retained from the parameter identification at 50 rpm.

## List of symbols

$A_{\text{geom}}$	Geometric surface area of electrode, m <sup>2</sup>
$a_j$	Activity of dissolved species $j$ , –
$a_{\text{surf},j}$	Activity of dissolved species $j$ at catalyst surface, –
$c_{\text{CO}_2(\text{diss})}^0$	Concentration of dissolved CO <sub>2</sub> in water, mol m <sup>-3</sup>
$c_{\text{CO}_2(\text{diss})}$	Concentration of dissolved CO <sub>2</sub> in electrolyte solution, mol m <sup>-3</sup>
$C_{\text{DL}}$	Double layer capacitance, $\mu\text{F cm}^{-2}$
$c_{\text{elyt}}$	Electrolyte concentration, mol m <sup>-3</sup>
$c_j, c_m$	Concentration of species $j$ or $m$ , mol m <sup>-3</sup>
$c_j^{\ominus}$	Standard concentration of species $j$ , mol m <sup>-3</sup>
$d$	Diffusion layer thickness, m
$D_j$	Diffusion coefficient of species $j$ , m <sup>2</sup> s <sup>-1</sup>
$E$	Potential, V
$E_{\text{ext}}$	External potential, V
$E_i^{00}$	Standard potential of reaction $i$ , V
$F$	Faraday constant, C mol <sup>-1</sup>
$FE$	Faradaic efficiency, –
$H_{\text{CO}_2}^{\text{CP}}$	Henry coefficient of CO <sub>2</sub> , mol m <sup>-3</sup> Pa <sup>-1</sup>
$h_m$	Substance specific parameter for ionic species $m$ for consideration of salting-out effect, m <sup>3</sup> kmol <sup>-1</sup>
$i$	Current density, A m <sup>-2</sup>
$i_F$	Faradaic current density, A m <sup>-2</sup>
$K_i$	Equilibrium constant of reaction $i$ , –
$k_{i,b}$	Backward reaction rate constant of reaction $i$ , mol m <sup>-2</sup> s <sup>-1</sup> (surface specific) and mol m <sup>-3</sup> s <sup>-1</sup> (volumetric)
$k_{i,f}$	Forward reaction rate constant of reaction $i$ , mol m <sup>-2</sup> s <sup>-1</sup> (surface specific) and mol m <sup>-3</sup> s <sup>-1</sup> (volumetric)
$N_j$	Molar transport flux of dissolved species $j$ , mol m <sup>-2</sup> s <sup>-1</sup>
$p$	Pressure, Pa
$p_{\text{CO}_2}$	Partial pressure of CO <sub>2</sub> , Pa
$\text{pH}_{\text{bulk}}$	pH of electrolyte bulk, –
$R$	Universal gas constant, J mol <sup>-1</sup> m <sup>-2</sup>
$r_i$	Surface specific reaction rate of surface reaction $i$ , mol m <sup>-2</sup> s <sup>-1</sup> and volumetric reaction rate of homogeneous reaction $i$ , mol m <sup>-3</sup> s <sup>-1</sup>
$R_{\text{int}}$	Internal resistance, $\Omega$
$\dot{S}_j$	Source term of species $j$ , mol m <sup>-3</sup> s <sup>-1</sup>
$T$	Temperature, K
$t$	Time, s
$u_j$	Mobility of species $j$ , s mol kg <sup>-1</sup>
$z_j$	Charge number of species $j$ , –

$\alpha_{\text{CO}_2\text{R}}$	Charge transfer coefficient for CO <sub>2</sub> R, –
$\alpha_{\text{HER}}$	Charge transfer coefficient for HER, –
$\Gamma$	Concentration of active surface sites, mol m <sup>-2</sup>
$\gamma_j$	Activity coefficient of species $j$ , –
$\Delta X$	Thickness of discretization element, m
$\eta_i$	Overpotential of reaction $i$ , V
$\theta_k$	Surface coverage of adsorbed species $k$ , –
$v$	Scan rate, mV s <sup>-1</sup>
$\nu_{j,i}$	Stoichiometric factor of species $j$ in reaction $i$ , –
$\sigma$	Ionic conductivity of electrolyte phase, S m <sup>-2</sup>
$\tau_{\text{diff}}$	Time constant of diffusive transport, s
$\phi$	Potential in electrolyte phase, V
[ ]	Free catalyst surface sites, –

## Acknowledgements

We are thankful to the German Research Foundation for funding this research in the framework of the Research Unit 2397 (KR 3850-6-2). We acknowledge support by the KIT-Publication Fund of the Karlsruhe Institute of Technology, Germany. Open Access funding enabled and organized by Projekt DEAL.

## Conflict of Interests

The authors declare no conflict of interest.

## Data Availability Statement

The data presented in the manuscript are openly available in the KITopen repository at DOI: 10.35097/1652.

**Keywords:** carbonation reaction · cyclic voltammetry · dynamic kinetic modelling · electrochemical CO<sub>2</sub> reduction · silver

- [1] S. Nitopi, E. Bertheussen, S. B. Scott, X. Liu, A. K. Engstfeld, S. Horch, B. Seger, I. E. L. Stephens, K. Chan, C. Hahn, J. K. Nørskov, T. F. Jaramillo, I. Chorkendorff, *Chem. Rev.* **2019**, *119*, 7610–7672.
- [2] Y. Hori, K. Kikuchi, S. Suzuki, *Chem. Lett.* **1985**, *14*, 1695–1698.
- [3] B. Kumar, M. Asadi, D. Pisasale, S. Sinha-Ray, B. A. Rosen, R. Haasch, J. Abiade, A. L. Yarin, A. Salehi-Khojin, *Nat. Commun.* **2013**, *4*.
- [4] J. K. Pedersen, T. A. A. Batchelor, A. Bagger, J. Rossmeisl, *ACS Catal.* **2020**, *10*, 2169–2176.
- [5] T. Asset, S. T. Garcia, S. Herrera, N. Andersen, Y. Chen, E. J. Peterson, I. Matanovic, K. Artyushkova, J. Lee, S. D. Minteer, S. Dai, X. Pan, K. Chavan, S. Calabrese Barton, P. Atanassov, *ACS Catal.* **2019**, *9*, 7668–7678.
- [6] G. Li, T. Yan, X. Chen, H. Liu, S. Zhang, X. Ma, *Energy Fuels* **2022**, *36*, 4234–4249.
- [7] F. Pan, Y. Yang, *Energy Environ. Sci.* **2020**, *13*, 2275–2309.
- [8] M. G. Kibria, J. P. Edwards, C. M. Gabardo, C. T. Dinh, A. Seifitokaldani, D. Sinton, E. H. Sargent, *Adv. Mater.* **2019**, *31*, e1807166.
- [9] J.-B. Vennekoetter, R. Sengpiel, M. Wessling, *Chem. Eng. J.* **2019**, *364*, 89–101.
- [10] T. Shinagawa, A. T. Garcia-Esparza, K. Takahashi, *Sci. Rep.* **2015**, *5*, 13801.
- [11] A. M. Limaye, J. S. Zeng, A. P. Willard, K. Manthiram, *Nat. Commun.* **2021**, *12*, 703.
- [12] M. Dunwell, W. Luc, Y. Yan, F. Jiao, B. Xu, *ACS Catal.* **2018**, *8*, 8121–8129.
- [13] E. L. Clark, J. Resasco, A. Landers, J. Lin, L.-T. Chung, A. Walton, C. Hahn, T. F. Jaramillo, A. T. Bell, *ACS Catal.* **2018**, *8*, 6560–6570.

- [14] U. Krewer, C. Weinzierl, N. Ziv, D. R. Dekel, *Electrochim. Acta* **2018**, *263*, 433–446.
- [15] B. J. M. Etzold, U. Krewer, S. Thiele, A. Dreizler, E. Klemm, T. Turek, *Chem. Eng. J.* **2021**, *424*, 130501.
- [16] U. Krewer, T. Vidakovic-Koch, L. Rihko-Struckmann, *ChemPhysChem* **2011**, *12*, 2518–2544.
- [17] D. Zhang, K. Zeng, *Ind. Eng. Chem. Res.* **2012**, *51*, 13825–13832.
- [18] J. G. Vos, M. T. M. Koper, *J. Electroanal. Chem.* **2018**, *819*, 260–268.
- [19] A. Goyal, G. Marcandalli, V. A. Mints, M. T. M. Koper, *J. Am. Chem. Soc.* **2020**, *142*, 4154–4161.
- [20] M. Löffler, P. Khanipour, N. Kulyk, K. J. J. Mayrhofer, I. Katsounaros, *ACS Catal.* **2020**, *10*, 6735–6740.
- [21] A. J. Bard, L. R. Faulkner, *Electrochemical methods: Fundamentals and applications*, 2<sup>nd</sup> edition, John Wiley & Sons, New York **2001**.
- [22] R. Casebolt, K. W. Kimura, K. Levine, J. A. Cimada DaSilva, J. Kim, T. A. Dunbar, J. Suntivich, T. Hanrath, *ChemElectroChem* **2021**, *8*, 681–688.
- [23] M. Röhe, F. Kubannek, U. Krewer, *ChemSusChem* **2019**, *12*, 2373–2384.
- [24] M. Röhe, A. Botz, D. Franzen, F. Kubannek, B. Ellendorff, D. Öhl, W. Schuhmann, T. Turek, U. Krewer, *ChemElectroChem* **2019**, *6*, 5671–5681.
- [25] N. Gupta, M. Gattrell, B. MacDougall, *J. Appl. Electrochem.* **2006**, *36*, 161–172.
- [26] C. Kim, L.-C. Weng, A. T. Bell, *ACS Catal.* **2020**, *10*, 12403–12413.
- [27] J. C. Bui, C. Kim, A. Z. Weber, A. T. Bell, *ACS Energy Lett.* **2021**, *6*, 1181–1188.
- [28] P. Schön, U. Krewer, *Electrochim. Acta* **2021**, *373*, 137523.
- [29] E. Barsoukov, J. R. Macdonald, *Applications*, 2nd ed. (Hoboken, NJ: John Wiley & Sons, Inc., 2005) **2005**.
- [30] U. Krewer, M. Christov, T. Vidakovic', K. Sundmacher, *J. Electroanal. Chem.* **2006**, *589*, 148–159.
- [31] M. Röhe, D. Franzen, F. Kubannek, B. Ellendorff, T. Turek, U. Krewer, *Electrochim. Acta* **2021**, *389*.
- [32] F. Bienen, D. Kopljar, S. Geiger, N. Wagner, K. A. Friedrich, *ACS Sustainable Chem. Eng.* **2020**, *8*, 5192–5199.
- [33] F. Bienen, D. Kopljar, A. Löwe, S. Geiger, N. Wagner, E. Klemm, K. A. Friedrich, *ACS Sustainable Chem. Eng.* **2020**, *8*, 13759–13768.
- [34] J. Geppert, P. Rose, S. Czioska, D. Escalera-Lopez, A. Boubnov, E. Saraci, S. Cherevko, J. D. Grunwaldt, U. Krewer, *J. Am. Chem. Soc.* **2022**, *144*, 13205–13217.
- [35] H. Hashiba, L.-C. Weng, Y. Chen, H. K. Sato, S. Yotsuhashi, C. Xiang, A. Z. Weber, *J. Phys. Chem.* **2018**, *122*, 3719–3726.
- [36] E. L. Clark, A. T. Bell, *J. Am. Chem. Soc.* **2018**, *140*, 7012–7020.
- [37] G. Marcandalli, M. C. O. Monteiro, A. Goyal, M. T. M. Koper, *Acc. Chem. Res.* **2022**, *55*, 1900–1911.
- [38] M. C. O. Monteiro, A. Mirabal, L. Jacobse, K. Doblhoff-Dier, S. C. Barton, M. T. M. Koper, *JACS Au* **2021**, *1*, 1915–1924.
- [39] T. Hatsukade, K. P. Kuhl, E. R. Cave, D. N. Abram, T. F. Jaramillo, *Phys. Chem. Chem. Phys.* **2014**, *16*, 13814–13819.
- [40] T. Burdyny, W. A. Smith, *Energy Environ. Sci.* **2019**, *12*, 1442–1453.
- [41] L.-C. Weng, A. T. Bell, A. Z. Weber, *Phys. Chem. Chem. Phys.* **2018**, *20*, 16973–16984.
- [42] S. Dieckhöfer, D. Öhl, J. R. C. Junqueira, T. Quast, T. Turek, W. Schuhmann, *Chem. - Eur. J.* **2021**, *27*, 5906–5912.
- [43] D. A. Henckel, M. J. Counihan, H. E. Holmes, X. Chen, U. O. Nwabara, S. Verma, J. Rodríguez-López, P. J. A. Kenis, A. A. Gewirth, *ACS Catal.* **2021**, *11*, 255–263.
- [44] M. Löffelholz, J. Osiewacz, A. Lüken, K. Perrey, A. Bulan, T. Turek, *Chem. Eng. J.* **2022**, *435*, 134920.
- [45] C. Delacourt, P. L. Ridgway, J. Newman, *J. Electrochem. Soc.* **2010**, *157*, B1902.
- [46] M. R. Singh, J. D. Goodpaster, A. Z. Weber, M. Head-Gordon, A. T. Bell, *Proc. Natl. Acad. Sci. USA* **2017**, *114*, E8812–E8821.
- [47] B. Jähne, G. Heinz, W. Dietrich, *J. Geophys. Res.* **1987**, *92*.
- [48] J. H. Wang, *J. Phys. Chem.* **1965**, *69*, 4412–4412.
- [49] M. Flury, T. F. Gimmi, in *Methods of Soil Analysis: Part 4 Physical Methods*, Vol. 5, **2002**, pp. 1323–1351.
- [50] K. G. Schulz, U. Riebesell, B. Rost, S. Thoms, R. E. Zeebe, *Mar. Chem.* **2006**, *100*, 53–65.
- [51] R. N. Roy, L. N. Roy, K. M. Vogel, C. Porter-Moore, T. Pearson, C. E. Good, F. J. Millero, D. M. Campbell, *Mar. Chem.* **1993**, *44*, 249–267.
- [52] S. Weisenberger, A. Schumpe, *AIChE J.* **1996**, *42*, 298–300.

---

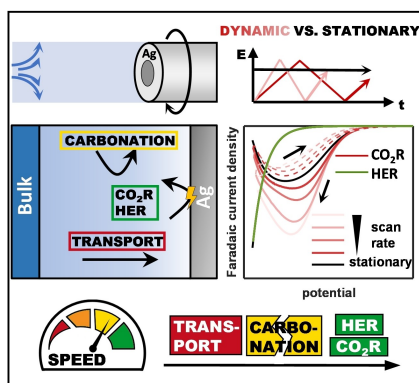
Manuscript received: August 4, 2023

Revised manuscript received: October 23, 2023

Version of record online: ■ ■ ■ ■ ■

# RESEARCH ARTICLE

Electrochemical CO<sub>2</sub> reduction on Ag electrodes suffers from slow transport and carbonation. This study reveals the strong temporal and spatial differences in concentrations and pH and the resulting strong impact on performance and Faradaic efficiency. Advice on quantifying and avoiding these effects is given.



I. Dorner, Dr. P. Röse, Prof. Dr.-Ing. U. Krewer\*

1 – 14

## Dynamic vs. Stationary Analysis of Electrochemical Carbon Dioxide Reduction: Profound Differences in Local States

